Electronic Supplementary Information for

Beneficial *vs.* Inhibiting Passivation by the Native Lithium Solid Electrolyte Interphase Revealed by Electrochemical Li^+ Exchange

Gustavo M. Hobold[1], Kyeong-Ho Kim[1] Betar M. Gallant[1,*]

[1]Department of Mechanical Engineering, Massachusetts Institute of Technology, Cambridge, MA 02139
*bgallant@mit.edu

Table of contents:

Supplementary methods

Diffusion-ordered spectroscopy nuclear magnetic resonance

Diffusion-ordered spectroscopy (DOSY) nuclear magnetic resonance (NMR) experiments were conducted to determine the diffusion coefficient of Li^+ in the electrolytes tested herein. Samples were prepared by dosing 500 µL of the desired electrolyte into a 5 mm NMR tube. Experiments were conducted at the ^7Li nucleus (194 MHz) at 298 K in a 400 MHz Bruker Avance-III HD Nanobay spectrometer operating with a Prodigy broad band observe probe. A typical pulse-field gradient spin-echo program was used without a lock solvent and shimmed to the highest ^1H-intensity peak in the electrolyte solvent. Parameters used were optimized depending on the electrolyte. Typical values included a diffusion delay (Δ, d20) of 150-1200 ms, gradient pulse duration (δ, 2 × d30) of up to 5 ms, gradient recovery delay (d16) of 200 µs, with a gradient strength varying from 4 to 96 % in 16 quadratic increments and a recycling delay (d1) of 2 s.

The integral of the Li^+ peak for each increment (S) was fitted with the gradient field strength to a three-parameter exponential expression, *i.e.*,

$$S(\delta) = A + S_0 \exp\left[-D(\gamma\delta G)\left(\Delta - \frac{\delta}{3}\right)\right],$$

from which D was obtained by a non-linear least square regression of the NMR data.

More precise measurements of chemical shift were conducted on the same spectrometer using a 6 ppm spectral width centered around 0 ppm, with an acquisition time of ~10 s and a recycling delay of 1 s, over 4 scans. All shifts were referenced externally to 1 M LiCl D_2O.

Scanning electron microscopy

Cells used for surface characterization (SEM) were taken into the glovebox after cycling and decrimped. The working electrode was removed from the assembly and soaked in 2 mL of dry DME or DMC for 3 minutes to remove excess salt from the surface before characterization. The clean electrode was then dried under vacuum, cut with stainless steel scissors. Images were collected with a Zeiss Merlin microscope at an accelerating voltage of 3 kV with a 200 pA current. Samples were transferred to the SEM without exposure to ambient air with a transfer vessel (Semilab) built for the Zeiss Merlin SEM airlock.

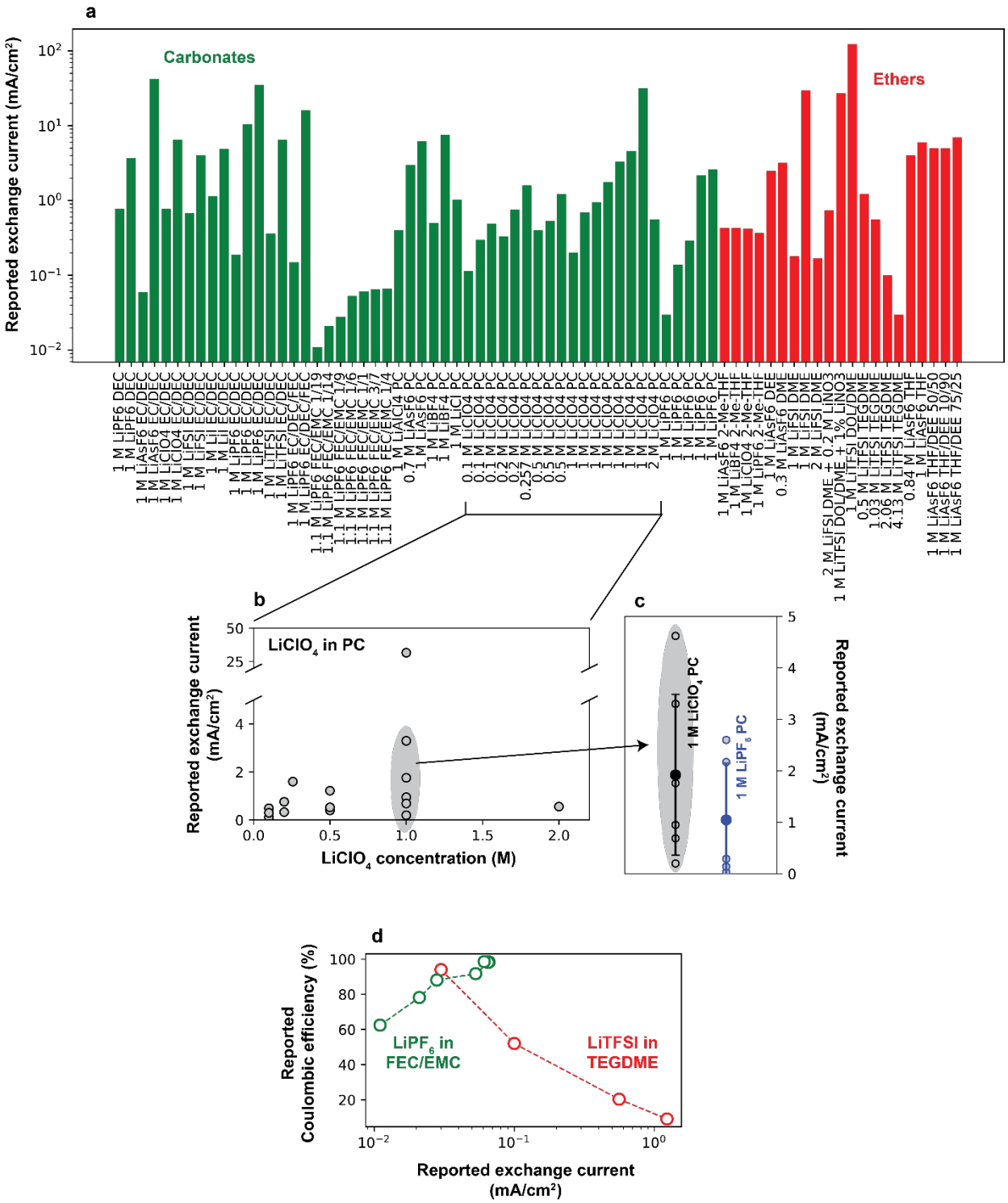

Fig. S1 (a) Compilation of published Li exchange current values, categorize by electrolyte. (b) Analysis of published values for Li exchange current for the $LiClO_4$-PC system, plotted as a function of concentration. (c) Plot of the values published for 1 M $LiClO_4$ PC and 1 M $LiPF_6$ PC. Filled markers indicate the mean across all values and error bars denote the standard deviation. Altogether, these figures compile the distinct values reported for Li^+ exchange and the disagreeing conclusions drawn by the Li community at large.

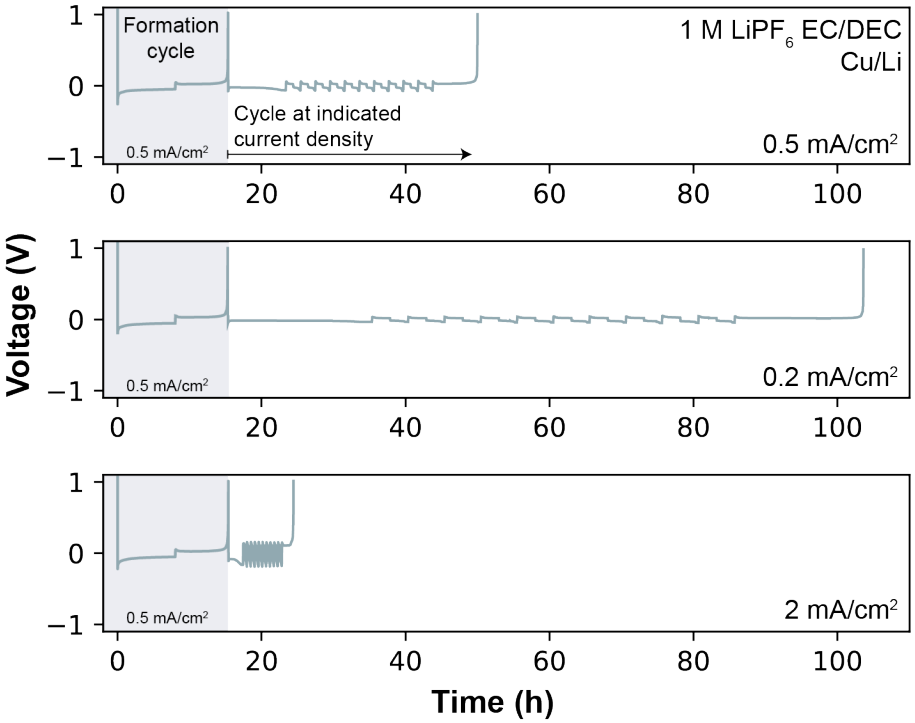

Fig. S2 Representative example of the Coulombic efficiency (CE) measurement protocol employed in this study based on Adams *et al.*[1], for 1 M $LiPF_6$ EC/DEC. The protocol includes a 4 mAh/cm^2 pre-formation cycle at 0.5 mA/cm^2 (highlighted). Then, at the indicated current density (typically 0.5 mA/cm^2, except for data shown in **Fig. 9**), a Li reservoir of 4 mAh/cm^2 was plated, followed by cycling of 1 mAh/cm^2 for 10 full cycles. Finally, full stripping was conducted to 1 V, at which point the CE was determined by the ratio of the total stripped over total plated capacity.

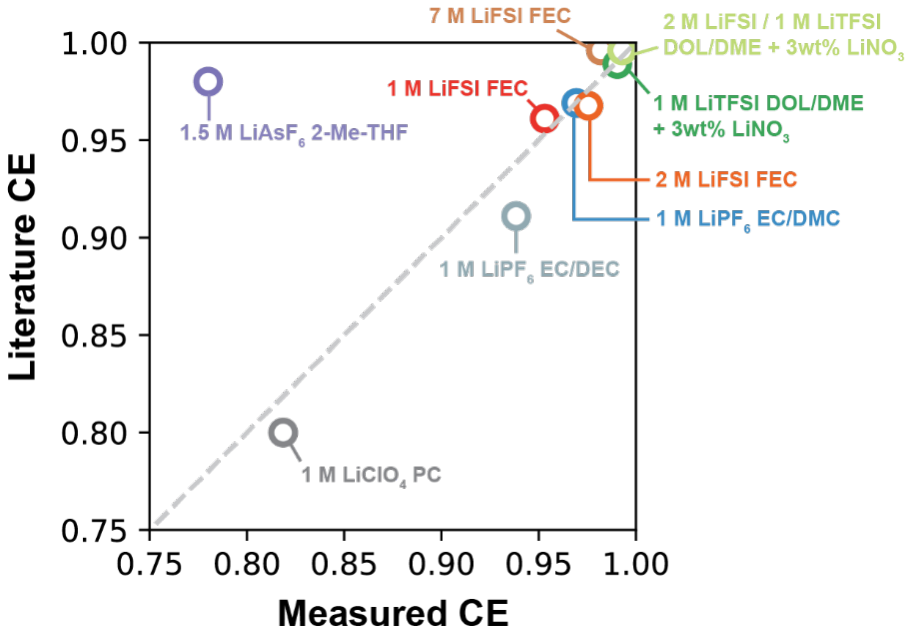

Fig. S3 CE measured herein compared to values originally reported elsewhere in literature (references in **Table S2**). The divergence observed between measured and previously-reported CE in 1.5 M $LiAsF_6$ 2-Me-THF is attributed to the instability between $LiAsF_6$ and 2-Me-THF,[2] which in turn results in data acquired in these electrolytes being challenging to reproduce.

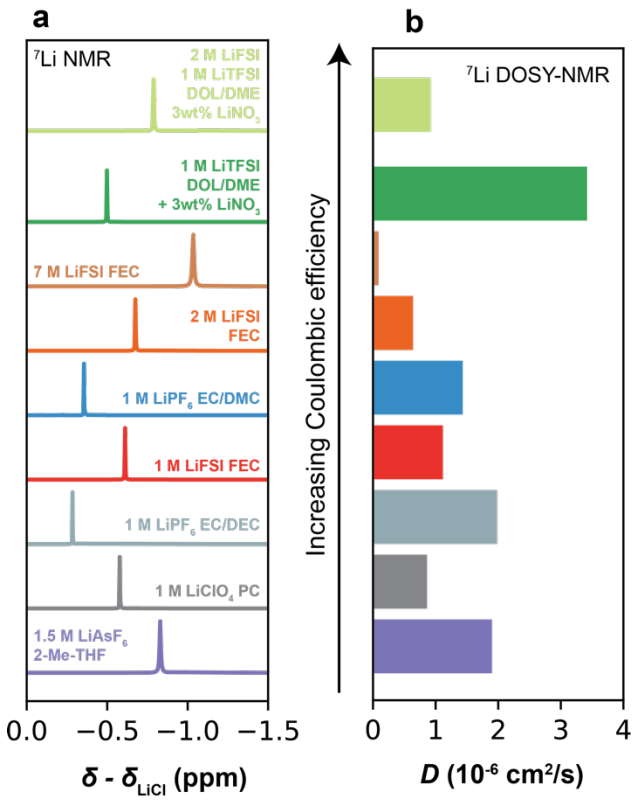

Fig. S4 Properties of electrolytes measured by NMR. (a) ^{7}Li NMR spectra of Li electrolytes examined in this study, externally referenced to 1 M LiCl D_2O at 0 ppm. (b) Li^+ diffusivity (D) of the same electrolytes measured by DOSY-NMR at 298 K.

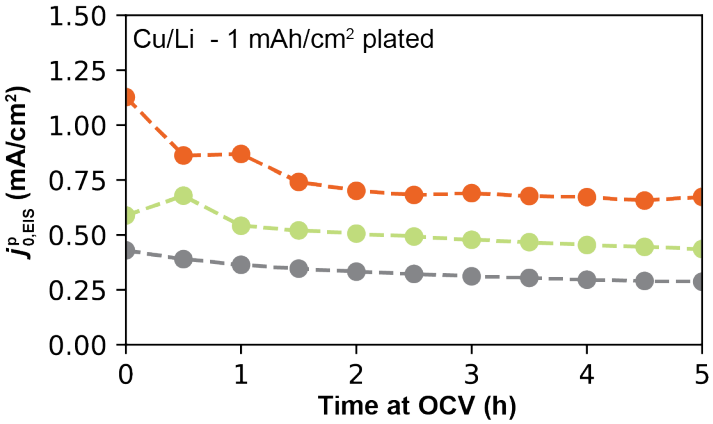

Fig. S5 Evolution of $j^{p}_{0,EIS}$ during a prolonged rest at OCV, measured from the EIS spectra collected in a Cu/Li cell after a single plating step of 1 mAh/cm^2.

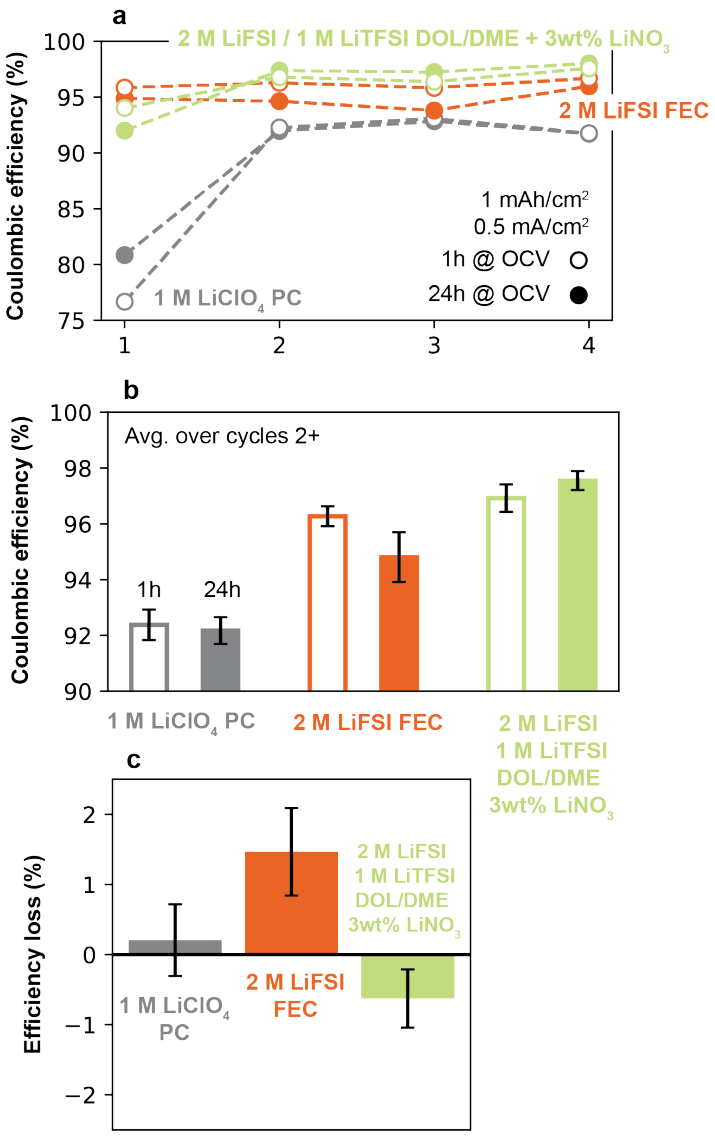

Fig. S6 (a) Coulombic efficiency as a function of cycle number obtained from 1 mAh/cm^2 galvanostatic cycles for 1 h and 24 h rest times between the plating and stripping half-cycles. (b) Average CE over cycles 2+, calculated from (a). Error bars denote the standard deviation. (c) Efficiency loss between 1 h and 24 h rest times. Positive values denote loss and negative values denote gain of efficiency. Error bars denote standard deviation. Altogether, the small CE variations even after 24 h of resting at OCV show that the SEI in the tested electrolytes are stable against the electrolyte for at least 24 h timescales. Thus, the choice of rest time (5 min) should not appreciably affect the results reported in the main text.

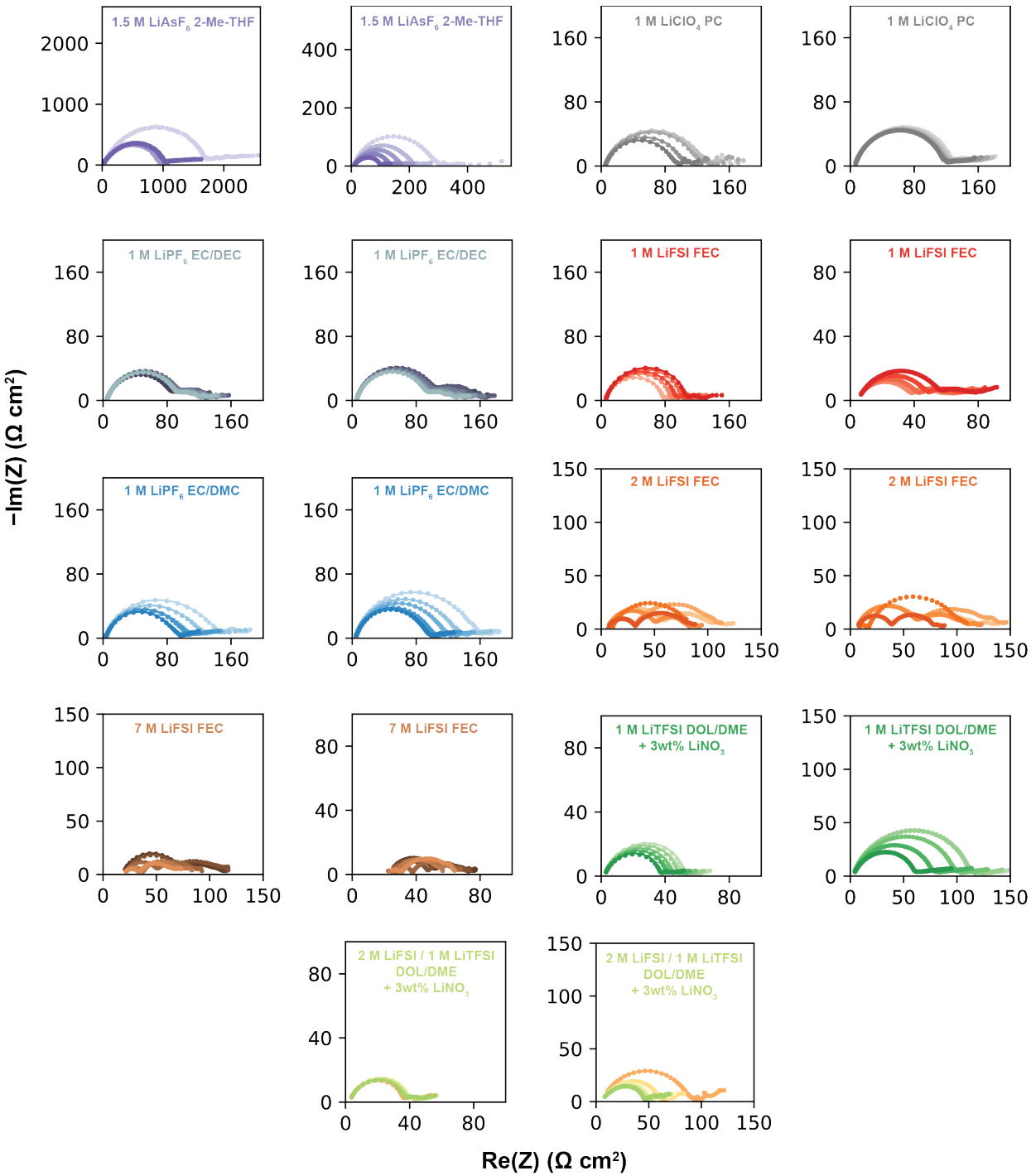

Fig. S7 Complete EIS spectra dataset for cycles 1-5 for all electrolytes considered herein, each measured in Li/Li cells after a full galvanostatic cycle of 1 mAh/cm^2 at 0.5 mA/cm^2. Duplicate plots for each electrolyte indicate repeat measurements under the same conditions.

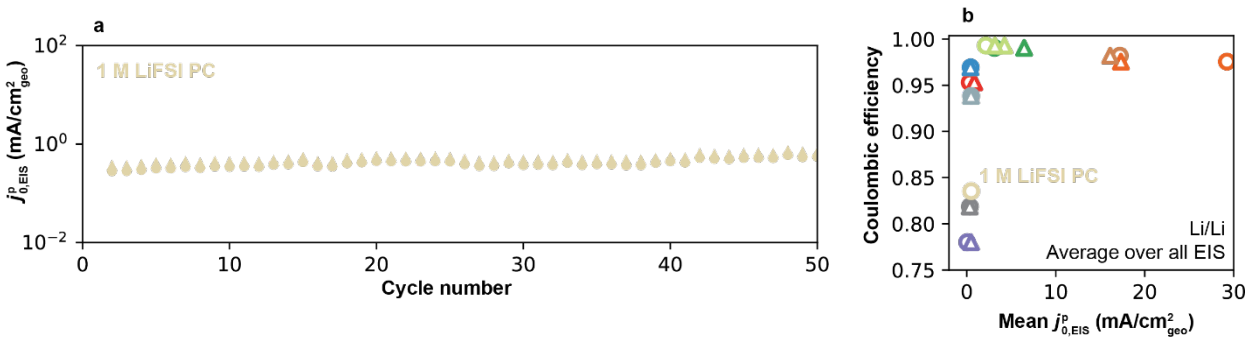

Fig. S8 (a) Analogous plot to **Fig. 3a**, for another low CE electrolyte (1 M LiFSI PC), showing constant and unchanging $j^{p}_{0,EIS}$, consistent with other Type 1 electrolytes. Triangles and round markers indicate replicate measurements. (b) Relationship between CE and $j^{p}_{0,EIS}$, where $j^{p}_{0,EIS}$ is averaged over all cycles in **Fig. 3a**. Color legend of electrolytes in **Fig. 3a**.

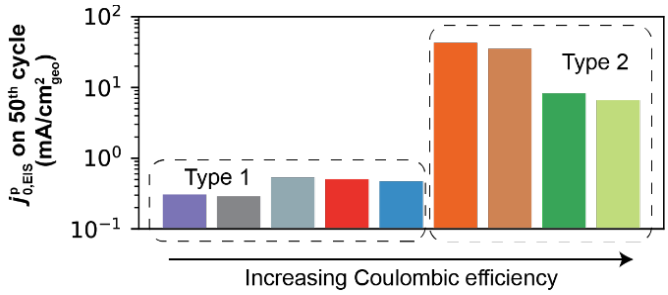

Fig. S9 $j^{p}_{0,EIS}$ measured on the 50th cycle (or last available before short-circuit) measured in Li/Li cells, organized by the electrolyte's CE.

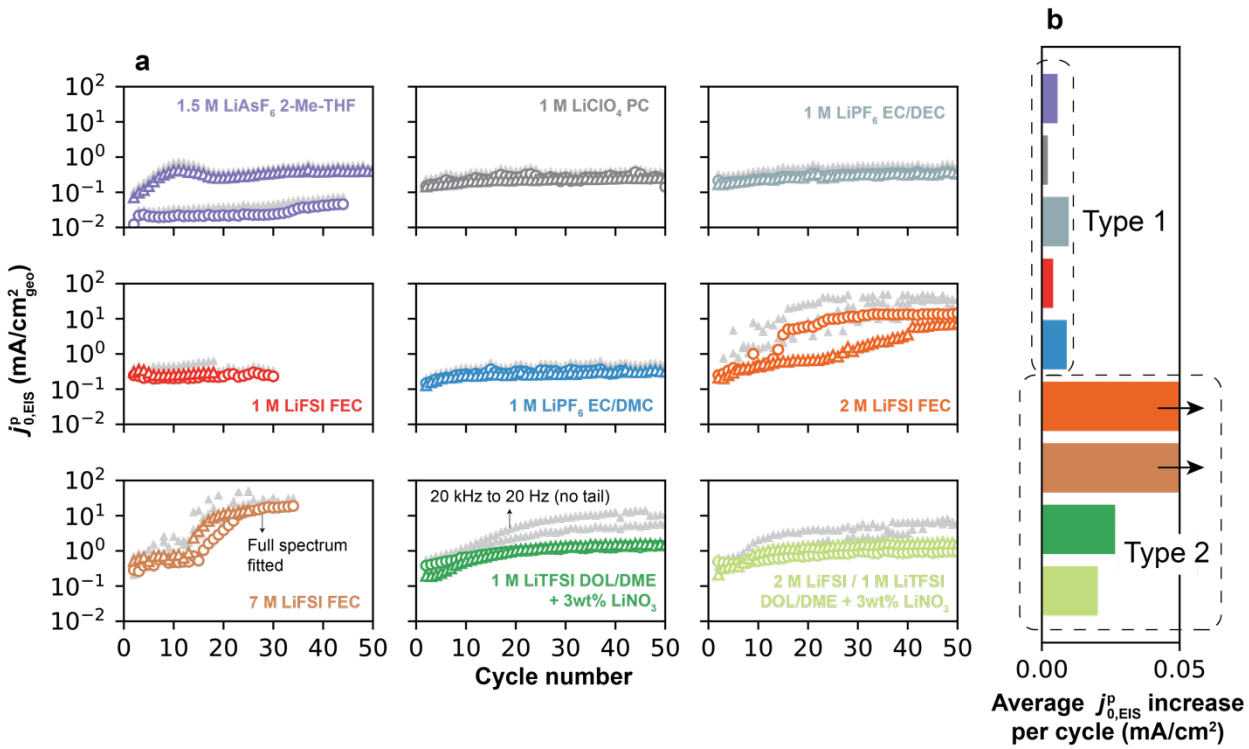

Fig. S10 Reproduction of Fig. 3a-b, in which $j_{0,EIS}^{p}$ is calculated by considering the entire collected EIS spectrum (20 kHz to 10 mHz, *i.e.*, including low frequency tail). Data fitted only on the inner semi-circle (20 kHz to 20 Hz) are shown as grey markers.

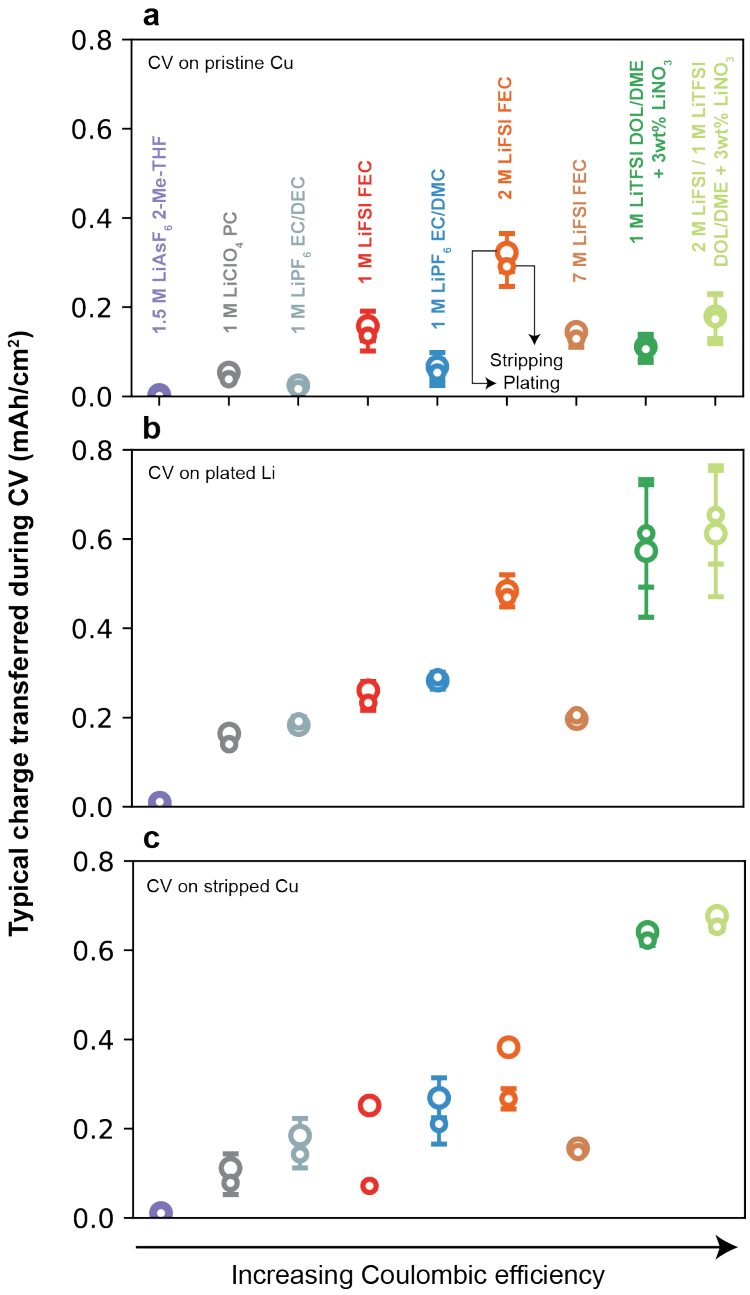

Fig. S11 Total charge transferred on an individual CV scan during the plating (cathodic scan) and stripping (anodic scan), with CVs performed on (a) pristine Cu, (b) after plating 1 mAh/cm^2 galvanostatically on Cu, (c) after full galvanostatic stripping of all previously plated Li. Error bars indicate the standard deviation over all CV scans.

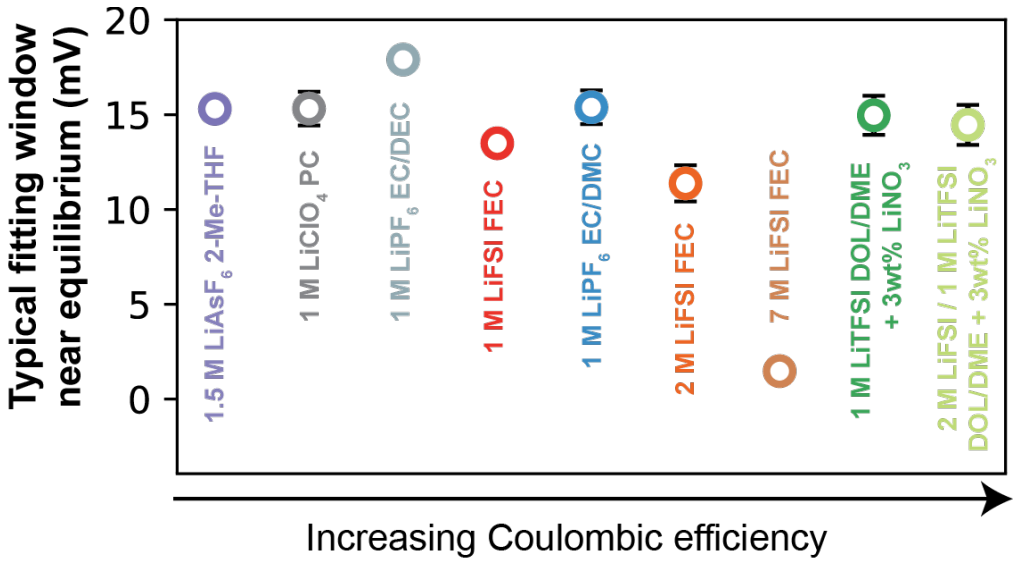

Fig. S12 Typical fitting windows used for determining $j_{0,CV}^{p}$ on plated Li at low overpotentials for all electrolytes considered herein. The fitting window was individually obtained on each scan for each electrolyte before fitting to ensure linearity within the region. Error bars indicate the standard deviation over all CV scans.

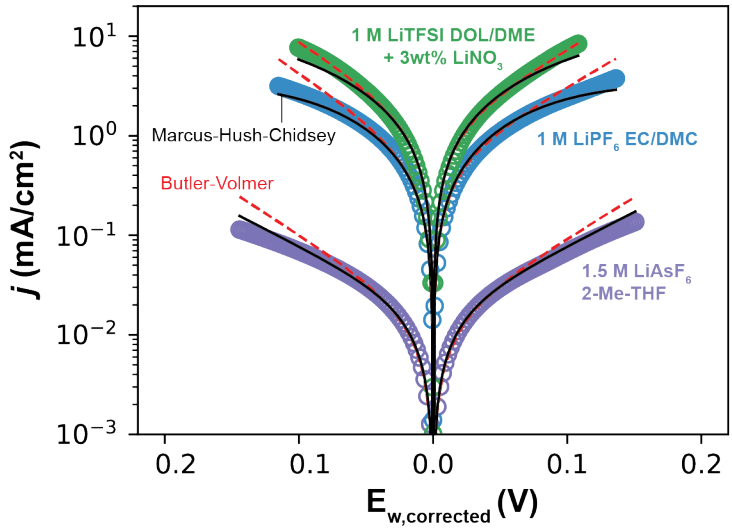

Fig. S13 Tafel plot of the 5th CV reverse scan on plated Li for 1.5 M $LiAsF_6$ 2-Me-THF, 1 M $LiPF_6$ EC/DMC and 1 M LiTFSI DOL/DME + 3wt% $LiNO_3$, along with curves fitted to the Butler-Volmer[3] (red dashed line) and Marcus-Hush-Chidsey[4] (black solid line) kinetics. Data for both models were fit in a 50 mV region around the equilibrium voltage.

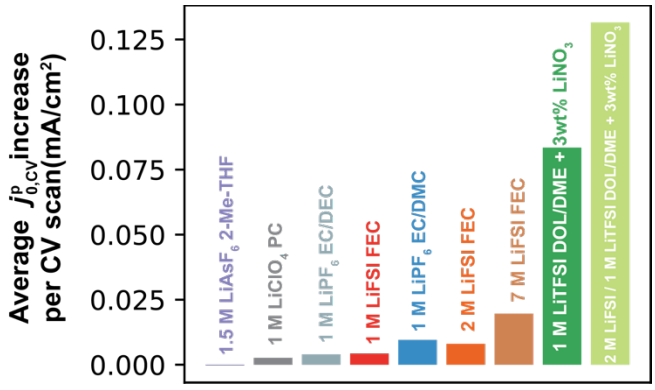

Fig. S14 Average variation in $j^{p}_{0,CV}$ over each CV scan on plated Li, calculated from data in **Fig. 6b**.

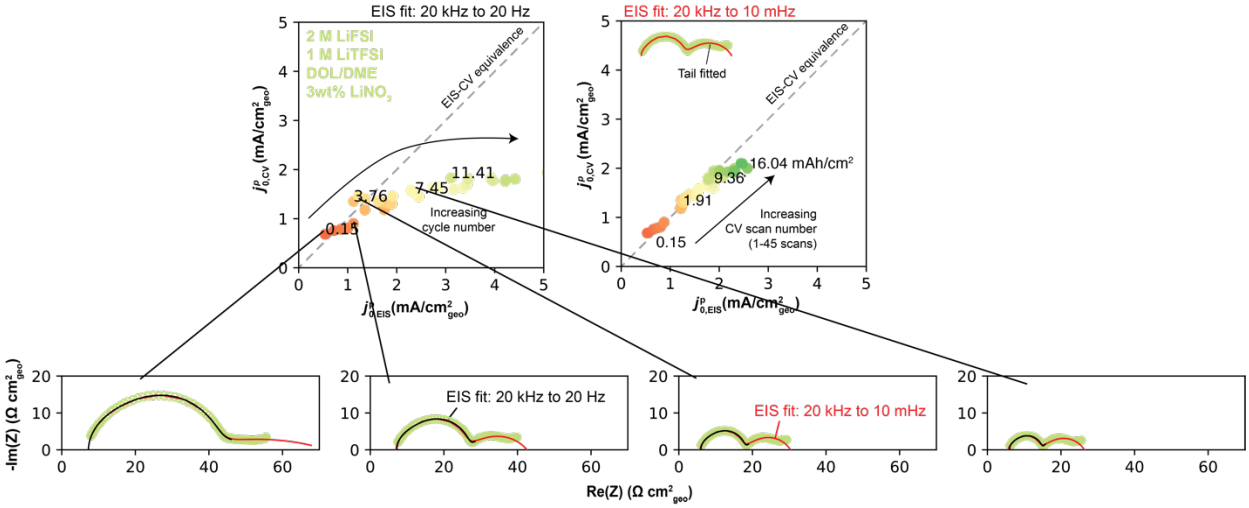

Fig. S15 EIS-CV equivalence plots for a Type 2 electrolyte (2 M LiFSI / 1 M LiTFSI DOL/DME + 3wt% $LiNO_3$), where $j^p_{0,EIS}$ is calculated disregarding the low frequency tail (20 kHz to 20 Hz, top left), and considering the low frequency tail (20 kHz to 10 mHz, top right). Text labels indicate the progression of the cumulative capacity in mAh/cm^2 cycled during the experiment. Bottom frames display the evolution of the EIS spectra over cycling, showing that $j^p_{0,CV}$ and $j^p_{0,EIS}$ start to disagree as the low frequency tail develops. Full methodology discussed in **ESI Note 3**.

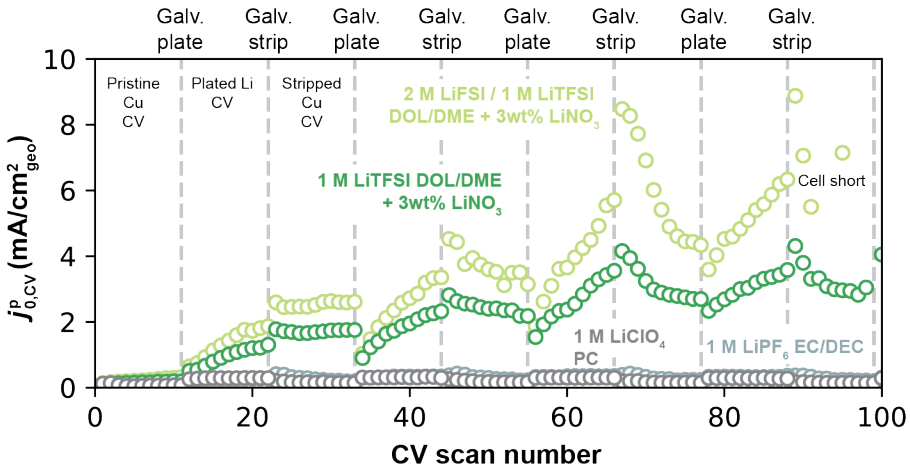

Fig. S16 Extended cycling with $j^p_{0,CV}$ measurements between half-cycles (following protocol shown in **Fig. 5**) of Cu/Li cells with 1 M $LiPF_6$ EC/DEC, 1 M LiTFSI DOL/DME + 3wt% $LiNO_3$, and 2 M LiFSI/1 M LiTFSI DOL/DME + 3wt% $LiNO_3$. The ether-based, high-CE electrolytes showed the same typical behavior of increasing $j^p_{0,CV}$ with cycling observed in EIS (**Fig. 3** and **Fig. 4**), whereas the carbonate-based electrolyte displayed a stable and low $j^p_{0,CV}$.

ESI Note 1 Analysis and fitting of electrochemical impedance spectroscopy spectra

The equivalent circuit used to fit all EIS spectra in this study consisted of a parallel resistor (R_{ct})-capacitor (C_{ct}) circuit in series with a parallel Warburg (Z_W)-capacitor (C_{SEI}) circuit and a resistor $R_{electrolyte}$ (**Fig. S17**). Because symmetric Li/Li cells were used to collect all EIS spectra, the impedances obtained from fitting **Fig. S17** to the raw data were normalized by the area of the two electrodes. A more general form of this circuit (containing up to 3 additional RC-circuits) was first suggested by Zaban *et al*.[5] We found that, for the electrolytes and conditions considered in this study, the simple model shown in **Fig. S17** is sufficient to fit the data with high fidelity, especially the high frequency semi-circle (> 20 Hz), as will be discussed later. Hence, we avoided making use of more complicated models to prevent unnecessary overfitting.

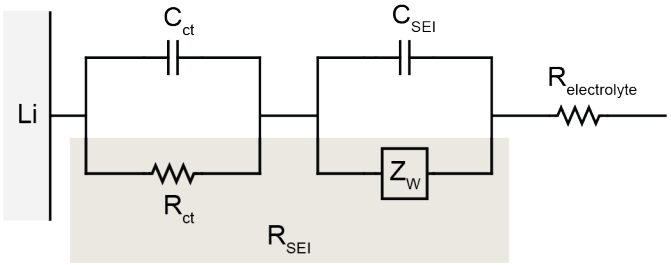

Fig. S17 Equivalent circuit used for fitting all electrochemical impedance spectroscopy spectra.

In this model, the inner $R_{ct}C_{ct}$-circuit represents the impedance to electrochemical charge-transfer (Li^0/Li^+ redox) at the Li-SEI interface,[6] whereas the outer $C_{SEI}Z_W$-circuit represents transport of Li^+ through the SEI.[7, 8] Fundamentally, the Warburg element models diffusion of an electrochemically-active species to/from an electrode,[9] and, in its general form, when the diffusion medium (here, the SEI) is finite, Z_W can be written as[5]

$$Z_W = W_1(i\omega W_2)^{-\gamma}\tanh[(i\omega W_2)^{\gamma}],$$

where: W_1 is the first Warburg coefficient, which is inversely proportional to Li^+ diffusivity of the medium (*i.e.*, SEI); W_2 is the second Warburg coefficient, which is proportional to the diffusion length; and $0 < \gamma \leq 1$ is a constant that is inversely proportional to the tortuosity of the medium to the transport of Li^+.[10] The full impedance of the equivalent circuit shown in **Fig. S17** is

$$Z = R_{\text{electrolyte}} + \left(i\omega C_{\text{ct}} + \frac{1}{R_{\text{ct}}}\right)^{-1} + \{i\omega C_{\text{SEI}} + (W_1[i\omega W_2]^{-\gamma}\tanh[(i\omega W_2)^{\gamma}])^{-1}\}^{-1}$$

Because the Warburg impedance is equivalent to that of RC-ladder circuits,[11] its frequency response can also be approximated by serializing multiple parallel RC-circuits (**Fig. S18**), an approach that is often employed in other works.[5, 12, 13] However, we chose to use the Warburg impedance in the circuit shown in **Fig. S17** for simplicity and for ease of interpretation, given that R_{SEI} from the RC-ladder circuit model approaches that of the circuit in **Fig. S17** upon inclusion of approximately 5 or more RC elements. For reference, converting these values into exchange current leads to ~0.33 mA/cm^2 compared to 0.35 obtained from the equivalent circuit in **Fig. S17**.

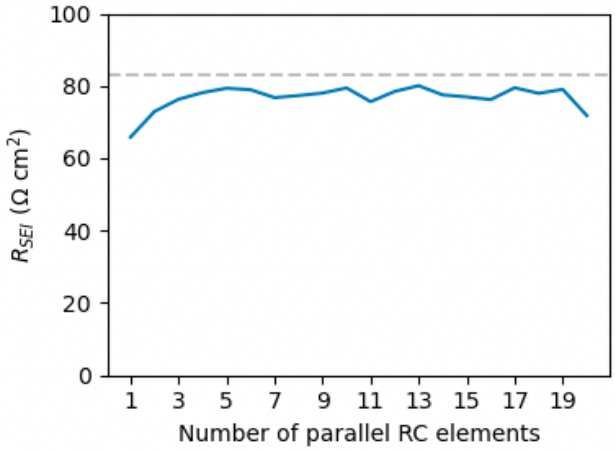

Fig. S18 SEI resistance R_{SEI} obtained by fitting equivalent circuits with a number of serialized parallel RC elements (blue line) along with R_{SEI} obtained by fitting to the circuit shown in **Fig. S17** (dashed line, R_{SEI} = 83.26 Ω cm^2); EIS performed after the first galvanostatic cycle in 1 M $LiPF_6$ EC/DMC.

In the low-frequency limit ($\omega \to 0$), the Warburg impedance Z_W behaves as a resistor such that $Z_W(\omega \to 0) = W_1$, and all capacitors exhibit infinite impedance. As such, at constant current, the impedance experienced by Li^+ through the SEI (*i.e.*, excluding electrolyte resistance) is

$$R_{\text{SEI}} = \frac{1}{2}\left(\lim_{\omega \to 0} Z - R_{\text{electrolyte}}\right) = \frac{1}{2}(R_{\text{ct}} + W_1)$$

where the 1/2 factor reflects the symmetry of the Li/Li cell and returns the impedance of one electrode. From R_{SEI}, an equivalent pseudo exchange current $j^{p}_{0,\text{EIS}}$ can be calculated through[3]

$$j_{0,\mathrm{EIS}}^{p} = \frac{kT}{neR_{\mathrm{SEI}}},$$

where k is Boltzmann's constant, T is the system's temperature (here taken as $T = 297$ K), $n = 1$ is the charge carried per ion (1 for Li^+), and e is the elementary charge.

An example of the fitted circuit is shown in **Fig. S19** (EIS spectra performed after the 5th galvanostatic cycle in 1 M $LiPF_6$ EC/DMC, see **Fig. 2b** for more details). Both the Nyquist (**Fig. S19a**) and Bode (**Fig. S19b**) plots show excellent agreement with the measured spectra. Similar agreement was found for all electrolytes tested herein, with a mean average percentage error between the fitted model and the experimental spectra typically below 10%, with over 80% of all fitted circuits displaying an error of less than 3% (**Fig. S20**). The model used here also allows the recovery of the charge-transfer resistance for Li^0/Li^+ redox (*e.g.*, $R_{ct} = 2.59$ Ω cm² for 1 M $LiPF_6$ in EC/DMC), which shows excellent agreement with transient voltammetry experiments in microelectrodes reported by another group in 1 M $LiPF_6$ EC/DEC ($R_{ct} = 2.5 \pm 0.2$ Ω cm²)[13] in spite of different surface conditioning.

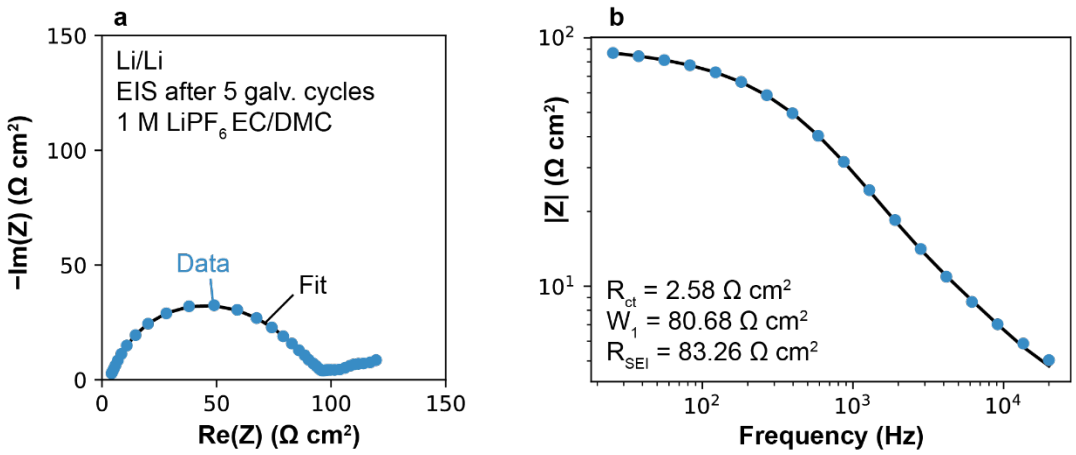

Fig. S19 (a) Nyquist and (b) Bode plots of fitted (solid line) and measured (marker) EIS spectra after the 5th cycle for 1 M $LiPF_6$ EC/DMC.

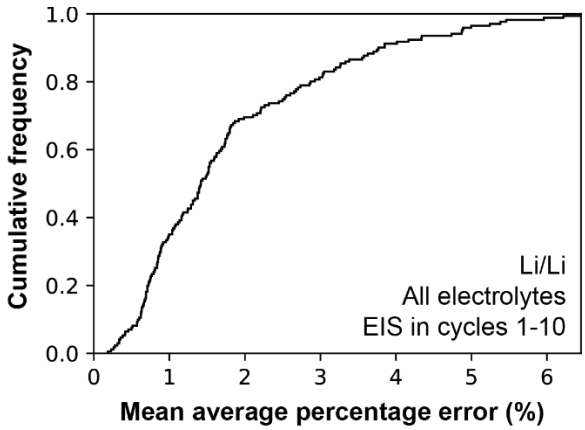

Fig. S20 Cumulative distribution of the mean average percentage error (MAPE) of the fitted circuit with respect to the measured EIS spectra for all electrolytes shown in **Fig. 3** (cycles 1-10). All fits show an average error of less than 6.5% with respect to the experimental data points, with the majority showing less than 2% error.

To make sure that the values we obtained from fitting are physically-consistent, we also verified that the fitted values R_{SEI} agree with the semi-circle width estimated from the raw data (**Fig. S21**).

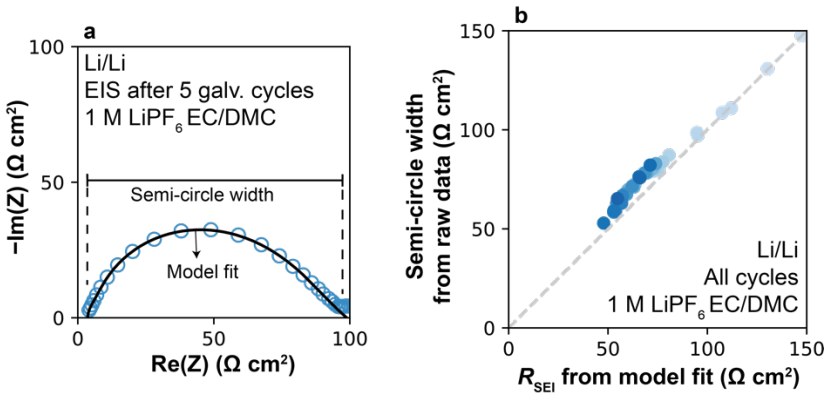

Fig. S21 (a) Magnification of a representative EIS spectrum collected after 5 galvanostatic cycles (1 mAh/cm^2, 0.5 mA/cm^2) in the 1 M $LiPF_6$ EC/DMC electrolyte, showing the semi-circle width along with the EIS model fit. (b) Agreement between R_{SEI} determined by the EIS model, compared to the semi-circle width estimated from the raw data.

ESI Note 2 Analysis and fitting of kinetic models to cyclic voltammetry data

Cyclic voltammetry (CV) data were acquired in two-electrode coin cells with a scan rate of 1 mV/s. We chose to use two-electrode coin cells in our studies to best represent real battery cell conditions, as well as to minimize electrolyte resistance due to the proximity (~100 µm) of the counter and working electrode. Electrolyte resistances were measured by EIS in separate Li/Li cells from an equivalent circuit (see **EIS Note 1**) and were typically << 10 Ω, with the exception of 7 M LiFSI, which displayed significant electrolyte resistance, typically >20 Ω, leading to iR drops of up to ~100 mV. Due to the high currents (> 5 mA) achieved in some systems, we performed iR correction for all measurements. **Fig. S22** demonstrates the effect of iR correction in select electrolytes. The electrolyte resistances measured by EIS along with the iR compensation at 50 mV is shown in **Fig. S23** for all electrolytes.

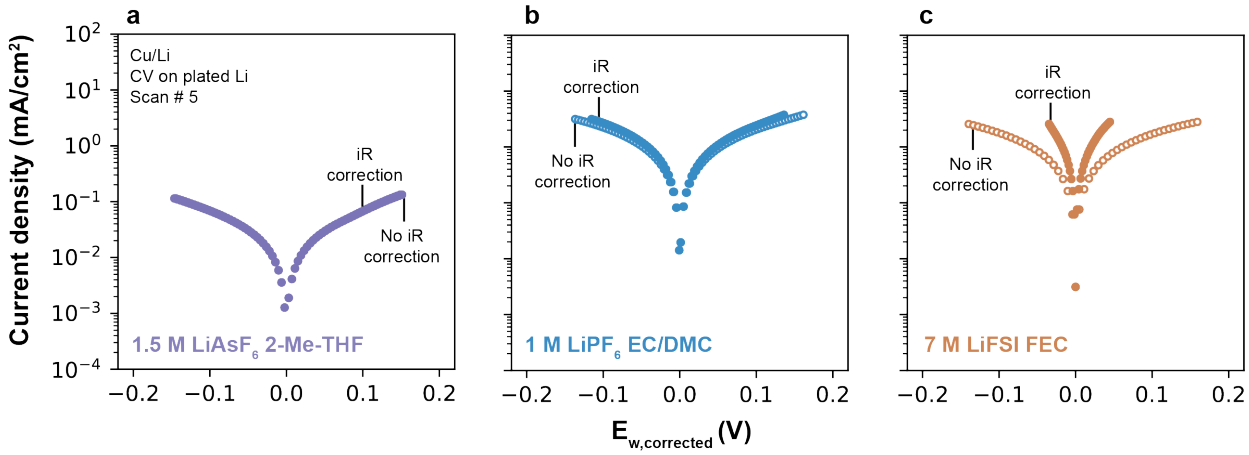

Fig. S22 Representative Tafel plots of (a) 1.5 M $LiAsF_6$ 2-Me-THF, (b) 1 M $LiPF_6$ EC/DEC and (c) 7 M LiFSI FEC before and after iR compensation, on the 5th CV scan on plated Li.

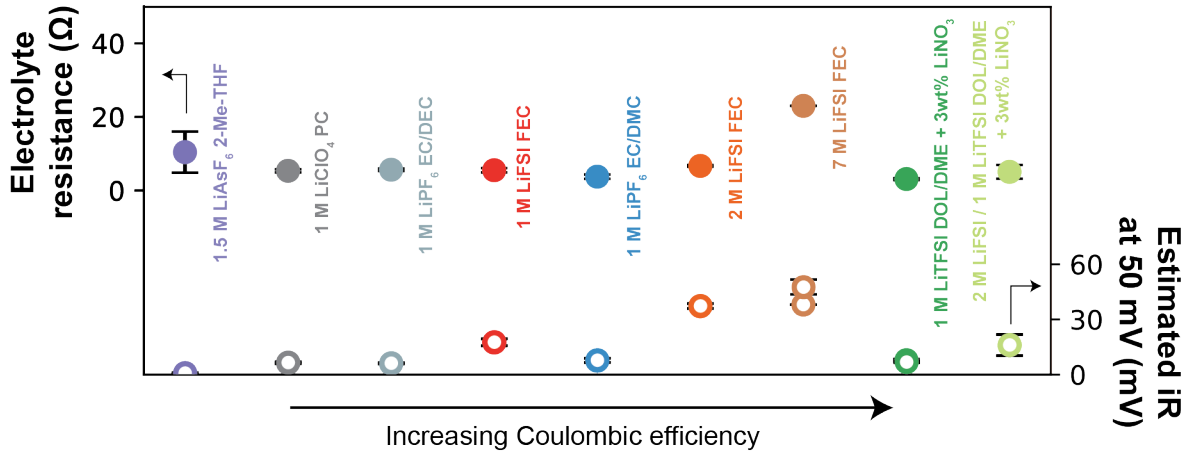

Fig. S23 Electrolyte resistance measured by EIS along with the iR compensation at 50 mV for all electrolytes considered in this study.

In order to make sure that the cyclic voltammetry data were not sensitive to scan rate, experiments were performed in Cu/Li cells after plating 4 mAh/cm^2 on Cu. The resulting Tafel plots of the 10th scan are shown in **Fig. S24** and show excellent agreement for 0.1 mV/s, 1 mV/s and 10 mV/s.

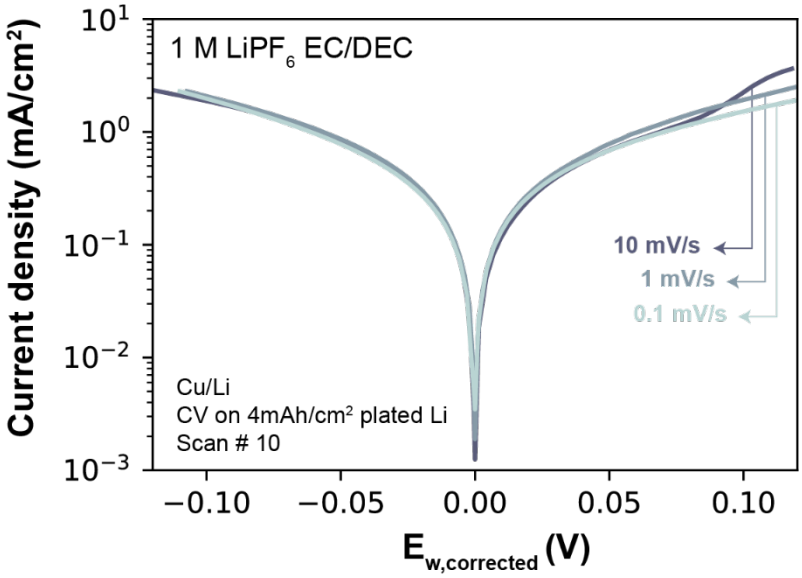

Fig. S24 Tafel plots obtained at 0.1 mV/s, 1 mV/s and 10 mV/s in Cu/Li cells after plating 4 mAh/cm^2 of Li on Cu, on the 10th CV scan. Excellent agreement was observed between all scan rates.

The kinetic analysis presented in this paper was performed on the reverse scan (*i.e.*, from -0.2 V to 1 V, or 0.2 V when the Cu electrode contained galvanostatically-plated Li), and the voltage was corrected to the equilibrium voltage such that $E_{w,corrected}(j = 0) = 0$ V.

After compensating for iR losses and correcting to the equilibrium voltage, an exchange current was determined by fitting the data to the linear low overpotential approximation, where the exchange current is proportional to the slope of the current-potential curve,[3] *i.e.*,

$$j = j_{0,CV}^{p} \frac{F}{RT} E_{w,\text{corrected}}$$

from which the representative $j_{0,CV}^{p}$ was obtained. This simplified modeling approach thus avoids the use of more detailed kinetic modeling or Tafel approximations at high overpotentials, which may be unphysical in interphase-dominated processes, and is the voltammetry equivalent of impedance spectroscopy.[3] The fitting window thus varied depending on the electrolyte, being narrower in electrolytes with high exchange current due to the narrower region where the current response is linear with potential (**Fig. S25**). This is better demonstrated in **Fig. S26**, where $j_{0,CV}^{p}$ is shown as a function of the fitting window. The low overpotential approximation becomes invalid at wider fitting windows, causing the estimated $j_{0,CV}^{p}$ to diverge from its value at low overpotentials. As such, 1 M LiTFSI DOL/DME + 3wt% $LiNO_3$ required a narrower window than 1 M $LiPF_6$ EC/DEC.

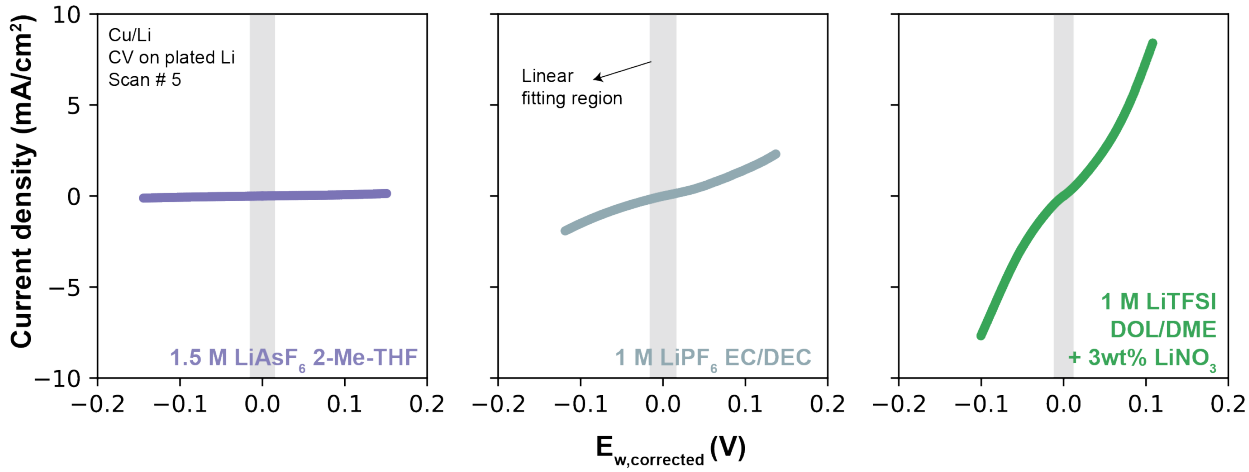

Fig. S25 Current-potential response of 1.5 M $LiAsF_6$ 2-Me-THF, 1 M $LiPF_6$ EC/DEC and 1 M LiTFSI DOL/DME + 3wt% $LiNO_3$, in order of increasing exchange current, with and without iR compensation. Grey region indicates window to which $j_{0,CV}^{p}$ is fit.

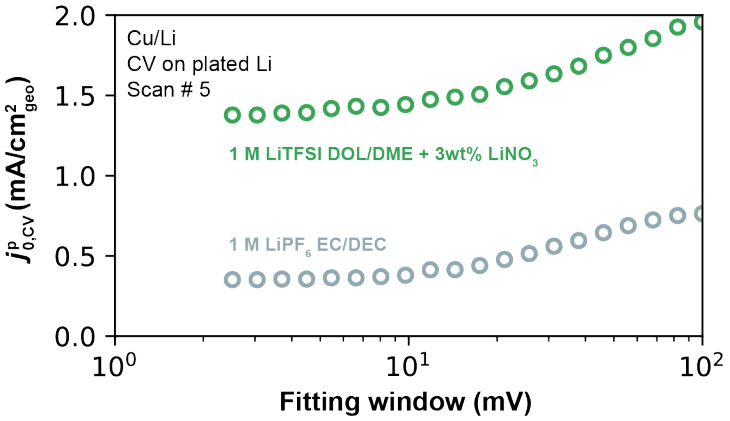

Fig. S26 $j_{0,CV}^{p}$ as a function of the voltage window used for fitting.

ESI Note 3 Equivalence between Li^+ exchange obtained by CV and EIS

Because EIS measures the current response to voltage oscillations around equilibrium, the exchange current obtained by EIS should be equivalent to that obtained by CV at low polarizations.[3] However, given the challenges associated with controlling for surface area discussed in the main text, it is expected that EIS and CV will show highest equivalency when a similar amount of Li has been cycled prior to computing j_0 using each method. In order to obtain the highest consistency between CV and EIS, a new experiment was designed, under which $j^p_{0,EIS}$ and $j^p_{0,CV}$ were measured under equivalent cycling conditions. The methodology is summarized in **Fig. S27** and consists of a Li/Li cell that undergoes a series of CV scans (from -200 mV to +200 mV) and galvanostatic cycles (1 mAh/cm^2). EIS spectra are collected before and after each CV scan. From these, $j^p_{0,EIS}$ corresponding to "before" and "after" CV were computed (following the methodology discussed in **ESI Note 1**) and averaged. $j^p_{0,CV}$ could also be computed (following **ESI Note 2**) using the data obtained during each CV scans. Thus, $j^p_{0,EIS}$ and $j^p_{0,CV}$ were computed in the same cell under equivalent cycling conditions, and showed excellent self-consistency across the two techniques (**Fig. 6c-d**). The limitations of the CV-EIS equivalence are further summarized in **Fig. S15**.

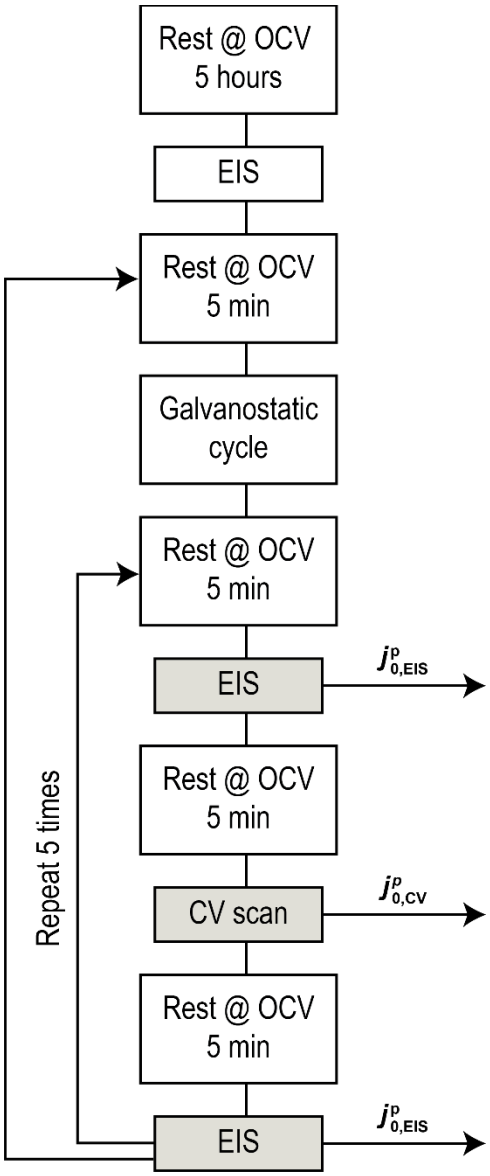

Fig S27. Flowchart of the experimental methodology used to derive the CV-EIS equivalence in Li/Li cells.

ESI Note 4 Transient evolution and stability of Li^+ exchange on Cu

The differences in Li^+ exchange between uncycled and cycled Cu shows, in **Fig. 8**, a tight per-cycle correlation to CE over several CV scans, before and after a galvanostatic cycle. Given these observations, we also investigated whether surface conditioning was a gradual, rather than the discrete process observed after a galvanostatic formation cycle. In this context, because CVs cycle a much smaller amount of Li per scan (~0.01 mA/cm^2 on pristine Cu for 1 M $LiPF_6$ EC/DEC, **Fig. S11**), they also allow a more gradual cycling of Li if performed uninterruptedly with no galvanostatic conditioning in-between, affording deeper analysis into the dynamic evolution of CE and $j^p_{0,CV}$ with cycling. **Fig**. **S28a** shows these dynamics, using 1 M $LiPF_6$ EC/DEC as the exemplar electrolyte. Examining this way, we observed a more continuous increase and correlation of $j^p_{0,CV}$ and CE with scan number, revealing a new insight: after a total capacity of ~7 mAh/cm^2 (corresponding to ~60 CV scans) was cycled, both CE and $j^p_{0,CV}$ stabilized in tandem, corresponding to $j^p_{0,CV}$ = 0.27 mA/cm^2. Interestingly, this value is equal to the $j^p_{0,CV}$ measured directly on plated Li (**Fig. 5c**), in spite of the fact that no Li reservoir was initially present in this experiment. In this more gradual cycling analysis, the transient evolution of $j^p_{0,CV}$ also shows the expected positive correlation with CE (**Fig. S28b**), thus consistent with our previous findings that higher CE is enabled by facile Li^+ exchange. More interestingly, the data show that, despite continued cycling, CE does not increase beyond a $j^p_{0,CV}$ stability point, revealing a limit to CE that is coupled to Li^+ exchange.

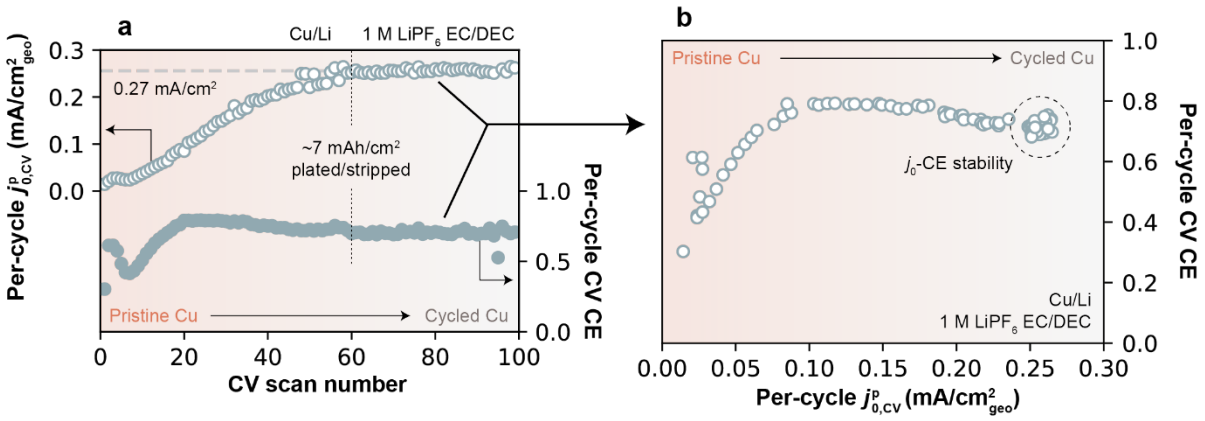

Fig. S28 Evolution and stability of Li^+ exchange. (a) $j^p_{0,CV}$ and CE obtained per cycle by uninterrupted CVs in Cu/Li cells, starting from pristine Cu. (b) $j^p_{0,CV}$-CE relationship derived from (a), revealing a stability point beyond which CE and $j^p_{0,CV}$ no longer increase.

Table S1 Li^0/Li^+ exchange current j_0 values reported in the literature with varying techniques and methodology. Experiments reported here were typically performed at room temperature (290-300 K) unless otherwise noted.

Electrolyte	Method to determine j_0	j_0 (mA/cm^2)	Other findings	Ref.
0.7 M $LiAsF_6$ in PC	Potentiostatic holds on 25 µm Ni microelectrode; Tafel analysis	3	CVs show reduced electrochemical activity after resting at OCV.	14
0.6-0.8 M $LiAsF_6$ in THF	Potentiostatic holds on 5 µm Ni microelectrode; Hickling analysis	4.0	j_0 shows Arrhenius behavior with temperature.	15, 16
1 M $LiClO_4$ in PC	CV at 150 mV/s on 5 µm Ni microelectrode; Tafel analysis	31.6	Reduced electrochemical activity observed resting at OCV. j_0 estimated to be 65 mA/cm^2 in zero-time OCV.	17
0.1-1 M $LiClO_4$ in PC	Potentiostatic holds around equilibrium on 0.08 cm^2 Li electrode; Linear *j-E* approximation at low polarization.	0.114-0.95	j_0 shows Arrhenius behavior with temperature.	18
0.1-1 M $LiClO_4$ in PC	Interrupted current method; Allen-Hickling analysis	0.3-1.76	Surface contamination on Li can drastically reduce j_0.	19

1 M $LiPF_6$ in PC 1 M $LiBF_4$ in PC 1 M $LiAlCl_4$ PC	Potentiostatic holds around equilibrium on 0.08 cm^2 Li electrode; Linear *j-E* approximation at low polarization.	0.29 0.5 0.4	j_0 shows Arrhenius behavior with temperature.	[20]
1 M LiCl in $AlCl_3$/PC	Potentiostatic holds around equilibrium on Li electrode; Linear *j-E* approximation at low polarization.	1.02	Experiments were also performed for other alkali metals	[21]
0.257 m LiClO in PC (ultradry)	Galvanostatic pulses on symmetric 0.38 cm^2 Li cell; Tafel analysis.	1.6-12	Time-dependent experiments, between 1 s to 1 h after exposure to electrolyte. Addition of H_2O drastically reduces j_0.	[22]
1 M $LiClO_4$ in PC	Li electrode; full methods not reported.	3.3	-	[23]
1 M $LiClO_4$ in PC	Electrochemical impedance spectroscopy on Li/Li cell.	0.2	Polarization experiments were also performed showing higher j_0.	[24]
1 M $LiAsF_6$ in THF/DEE	CV at 50 mV/s on 25-40 µm Ni microelectrode; Allen-Hickling analysis.	2.5-7	Varying proportions of DEE in THF used (0-100%).	[25]

0.3 M $LiAsF_6$ DME	CV at 20 mV/s and potentiostatic holds on 25-50 µm Ni microelectrode; Allen-Hickling analysis.	3.2	j_0 is lower in polyethers than in pure DME.	26
2 M LiFSI in DME 2 M LiFSI in DME + 0.2 M $LiNO_3$	CV at 1 mV/s in Li/Li coin cell; Tafel analysis.	0.17* 0.74*	Suggests high j_0 beneficial to CE. *values taken as reported, but j_0 values and Tafel plots reported are not consistent with each other.	27
1 M $LiAsF_6$ in EC/DEC 1 M $LiPF_6$ in EC/DEC 1 M $LiClO_4$ in EC/DEC 1 M LiI in EC/DEC 1 M LiTFSI in EC/DEC 1 M LiFSI in EC/DEC 1 M LiFSI in DME 1 M $LiPF_6$ in EC/DEC/FEC 1 M $LiPF_6$ in DEC 1 M $LiPF_6$ in PC	Electrochemical impedance spectroscopy on Li/Li cell / Transient voltammetry at >10 V/s on 12.5 µm W microelectrode; Marcus analysis.	0.06 / 42.3 0.19 / 10.4 0.78 / 6.5 1.15 / 4.9 0.36 / 6.5 0.68 / 4.0 0.18 / 29.8 0.15 / 16.0 0.78 / 3.7 0.03 / 2.6	j_0 obtained with SEI (EIS) is much lower than intrinsic Li^0/Li^+ redox kinetics (transient voltammetry)	13
1 M $LiPF_6$ in PC 1 M $LiAsF_6$ in PC 1 M $LiBF_4$ in PC 1 M $LiClO_4$ in PC 1 M $LiPF_6$ in 2-Me-THF 1 M $LiAsF_6$ in 2-Me-THF 1 M $LiBF_4$ in 2-Me-THF 1 M $LiClO_4$ in 2-Me-THF	CV at 20 mV/s on 100 µm Ni microelectrode; Allen-Hickling analysis.	2.17 6.20 7.51 4.62 0.37 0.43 0.43 0.42	Suggests low j_0 beneficial to CE	28

1 M $LiPF_6$ in EC/DEC 1 M LiTFSI in DOL/DME 1 M LiTFSI in DOL/DME + 1% $LiNO_3$	CV at 200 mV/s on 25 µm W microelectrode; Tafel analysis.	35 123 27	Suggests low j_0 beneficial to CE	29
1 M $LiPF_6$ in EC/DEC 1 M LiTFSI in DOL/DME + 1% $LiNO_3$	CV at 200 mV/s on 25 µm W microelectrode.	High Low	Suggests low j_0 beneficial to CE. Precise values for j_0 not reported.	30
1 M LiTFSI in DOL-DME + 1 wt% $LiNO_3$ and polymer coating: No coating PDMS PEO PU PVDF PVDF-HFP SHP	CV at 200 mV/s on 25 µm W microelectrode; Tafel analysis.	27 5 22 20 27 39 27	More polar coatings correlate with higher j_0.	31
1 M $LiPF_6$ in FEC/FEMC/HFE 1 M $LiPF_6$ in EC/DMC 1 M $LiPF_6$ in FEC/DMC 4 M LiFSI in DME	Potentiostatic holds around equilibrium on Li electrode in Li/Li coin cells; Tafel analysis.	Precise values not reported	Suggests high j_0 beneficial to CE.	32
1.1 M $LiPF_6$ in FEC/EMC with ratios: 1/19 1/14 1/9 1/6 1/4 3/7 1/1	CV at 1 mV/s in Li/Cu coin cells; Tafel analysis.	0.011 0.021 0.028 0.053 0.066 0.065 0.061	Suggests high j_0 beneficial to CE.	33

1 M $LiPF_6$ in PC (pristine) Pristine + 0.1 M $SiCl_4$ Pristine + 0.2 M $SiCl_4$ Pristine + 0.5 M $SiCl_4$ Pristine + 1 M $SiCl_4$	CV at 1 mV/s in Li/Li coin cells; Tafel analysis.	0.14 1 0.87 not reported not reported	Suggests high j_0 beneficial to CE.	[34]
Li(G4)[TFSI] $Li(G4)_2$[TFSI] $Li(G4)_4$[TFSI] $Li(G4)_8$[TFSI]	Voltammetry; full methods not reported.	0.03 0.10 0.56 1.23	Suggests low j_0 beneficial to CE.	[35]

Table S2 Li Coulombic efficiency (CE) of the electrolytes tested in this paper as reported by the original authors. A graphical comparison these values and the ones measured herein using the preformation-reservoir cycling protocol (**Fig. S2**) is shown in **Fig. S3**.

Electrolyte	Reported CE	Measured CE	Notes	Ref.
1.5 M $LiAsF_6$ 2-Me-THF	98%	78.0%	Reservoir cycling to depletion, 0.94 mAh/cm^2 reservoir, 0.3 mAh/cm^2 cycles, 5 mA/cm^2.	[36]
1 M $LiClO_4$ PC	80%	81.9%	First-cycle CE, brass current collector, 2.5 mA/cm^2, 1.25 mAh/cm^2.	[37]
1 M $LiPF_6$ EC/DEC	91.1%	93.8%	Average over 40 cycles, 1 mAh/cm^2, 1 mA/cm^2.	[38]
1 M LiFSI FEC	96.1%	95.3%	Average over 100 full cycles, 0.25 mAh/cm^2, 0.25 mA/cm^2.	[39]
1 M $LiPF_6$ EC/DMC	89%	96.9%	Average over ~40 full cycles, 1 mAh/cm^2, 0.5 mAh/cm^2.	[40]
2 M LiFSI FEC	96.76%	97.5%	Average over 100 full cycles, 0.25 mAh/cm^2, 0.25 mA/cm^2.	[39]
7 M LiFSI FEC	99.6%	98.2%	Average over 100 full cycles, 0.25 mAh/cm^2, 0.25 mA/cm^2.	[39]
1 M LiTFSI DOL/DME + 3wt% $LiNO_3$	98.94%	99.0%	Pre-formation (5 mAh/cm^2) and reservoir cycling.	[41]
2 M LiFSI / 1 M LiTFSI DOL/DME + 3wt% $LiNO_3$	99.6%	99.3%	Pre-formation (5 mAh/cm^2) and reservoir cycling.	[41]

Supplemental references

1. B. D. Adams, J. Zheng, X. Ren, W. Xu and J. G. Zhang, *Adv. Energy Mater.*, 2018, **8**.
2. D. Aurbach, A. Zaban, Y. Gofer, O. Abramson and M. Ben-Zion, *J. Electrochem. Soc.*, 1995, **142**, 687-696.
3. A. J. F. L. R. J. W. Bard and Sons, *Electrochemical methods : fundamentals and applications*, John Wiley & Sons, Hoboken, 2007.
4. Y. Zeng, R. Smith, P. Bai and M. Z. Bazant, *Journal*, 2014, arXiv:1407.5370.
5. A. Zaban, E. Zinigrad and D. Aurbach, *J. Phys. Chem.*, 1996, **100**, 3089-3101.
6. A. J. Bard and L. R. Faulkner, *Electrochemical Methods: Fundamentals and Applications*, Wiley, 2000.
7. R. Guo and B. M. Gallant, *Chem. Mater.*, 2020, **32**, 5525-5533.
8. A. V. Churikov, I. M. Gamayunova and A. V. Shirokov, *J. Solid State Electrochem.*, 2000, **4**, 216-224.
9. D. D. Macdonald, *Electrochim. Acta*, 2006, **51**, 1376-1388.
10. T. Pajkossy, *J. Electroanal. Chem.*, 1991, **300**, 1-11.
11. J. C. Wang, *J. Electrochem. Soc.*, 1987, **134**, 1915-1920.
12. D. T. Boyle, W. Huang, H. Wang, Y. Li, H. Chen, Z. Yu, W. Zhang, Z. Bao and Y. Cui, *Nat. Energy*, 2021, **6**, 487-494.
13. D. T. Boyle, X. Kong, A. Pei, P. E. Rudnicki, F. Shi, W. Huang, Z. Bao, J. Qin and Y. Cui, *ACS Energy Lett.*, 2020, **5**, 701-709.
14. D. Pletcher, J. F. Rohan and A. G. Ritchie, *Electrochim. Acta*, 1994, **39**, 2015-2023.
15. J. D. Genders, W. M. Hedges and D. Pletcher, *J. Chem. Soc. Faraday Trans.*, 1984, **80**, 3399-3408.
16. W. M. Hedges and D. Pletcher, *J. Chem. Soc. Faraday Trans.*, 1986, **82**, 179-188.
17. M. W. Verbrugge and B. J. Koch, *J. Electroanal. Chem.*, 1994, **367**, 123-129.
18. S. G. Meibuhr, *J. Electrochem. Soc.*, 1970, **117**, 56.
19. R. F. Scarr, *J. Electrochem. Soc.*, 1970, **117**, 295-&.
20. S. G. Meibuhr, *J. Electrochem. Soc.*, 1971, **118**, 1320-&.
21. J. Jorne and C. W. Tobias, *J. Electrochem. Soc.*, 1974, **121**, 994-1000.
22. J. N. Butler, D. R. Cogley and J. C. Synnott, *J Phys Chem-Us*, 1969, **73**, 4026-&.
23. I. Epelboin, M. Froment, M. Garreau, J. Thevenin and D. Warin, *J. Electrochem. Soc.*, 1980, **127**, 2100-2104.
24. S. Morzilli, F. Bonino and B. Scrosati, *Electrochim. Acta*, 1987, **32**, 961-964.
25. K. S. Aojula, J. D. Genders, A. D. Holding and D. Pletcher, *Electrochim. Acta*, 1989, **34**, 1535-1539.
26. J. Xu and G. C. Farrington, *J. Electrochem. Soc.*, 1995, **142**, 3303-3309.
27. X. Q. Zhang, X. Chen, L. P. Hou, B. Q. Li, X. B. Cheng, J. Q. Huang and Q. Zhang, *ACS Energy Lett.*, 2019, **4**, 411-416.
28. R. Tao, X. Bi, S. Li, Y. Yao, F. Wu, Q. Wang, C. Zhang and J. Lu, *ACS. Appl. Mater. Interfaces*, 2017, **9**, 7003-7008.
29. F. Shi, A. Pei, A. Vailionis, J. Xie, B. Liu, J. Zhao, Y. Gong and Y. Cui, *Proceedings of the National Academy of Sciences*, 2017, **114**, 12138.

30. F. F. Shi, A. Pei, D. T. Boyle, J. Xie, X. Y. Yu, X. K. Zhang and Y. Cui, *P Natl Acad Sci USA*, 2018, **115**, 8529-8534.
31. J. Lopez, A. Pei, J. Y. Oh, G.-J. N. Wang, Y. Cui and Z. Bao, *J. Am. Chem. Soc*, 2018, **140**, 11735-11744.
32. X. L. Fan, L. Chen, O. Borodin, X. Ji, J. Chen, S. Hou, T. Deng, J. Zheng, C. Y. Yang, S. C. Liou, K. Amine, K. Xu and C. S. Wang, *Nat. Nanotechnol.*, 2018, **13**, 1191-1191.
33. C. C. Su, M. He, J. Shi, R. Amine, J. Zhang and K. Amine, *Angew. Chem.*, 2020, **59**, 18229-18233.
34. Q. Zhao, Z. Y. Tu, S. Y. Wei, K. H. Zhang, S. Choudhury, X. T. Liu and L. A. Archer, *Angew. Chem.*, 2018, **57**, 992-996.
35. Y. Liu, X. Xu, M. Sadd, O. O. Kapitanova, V. A. Krivchenko, J. Ban, J. Wang, X. Jiao, Z. Song, J. Song, S. Xiong and A. Matic, *Adv Sci (Weinh)*, 2021, **8**, 2003301.
36. J. L. Goldman, R. M. Mank, J. H. Young and V. R. Koch, *J. Electrochem. Soc.*, 1980, **127**, 1461-1467.
37. R. Selim and P. Bro, *J. Electrochem. Soc.*, 1974, **121**, 1457-1457.
38. M. Genovese, A. J. Louli, R. Weber, R. J. Sanderson, M. B. Johnson and J. R. Dahn, *J. Electrochem. Soc.*, 2018, **165**, A3000-A3013.
39. L. Suo, W. Xue, M. Gobet, S. G. Greenbaum, C. Wang, Y. Chen, W. Yang, Y. Li and J. Li, *P Natl Acad Sci USA*, 2018, **115**, 1156-1161.
40. E. Markevich, G. Salitra, F. Chesneau, M. Schmidt and D. Aurbach, *ACS Energy Lett.*, 2017, **2**, 1321-1326.
41. F. Qiu, X. Li, H. Deng, D. Wang, X. Mu, P. He and H. Zhou, *Adv. Energy Mater.*, 2019, **9**, 1803372-1803372.